

Figures of Merit for Light Bucket Mirrors

Bruce D. Holenstein¹, Richard J. Mitchell¹, and Robert H. Koch²

¹Gravic, Inc., Malvern, PA;

²Department of Physics and Astronomy, University of Pennsylvania, Philadelphia

Introduction

Aberrations of the surface of a mirror have multiple expressions. “Light bucket” mirrors challenge traditional Gaussian- and diffraction-oriented aberration theory due to large amplitude, caustic ray-crossing aberrations. Typical light bucket mirrors may be made of metal, epoxy, foam glass, tessellated segments, and other techniques (Genet 2009) and have many waves of aberration. What is needed is a method to characterize the suitability of light bucket mirrors for an intended purpose, whether that be diaphragm-limiting photometry, lunar occultations, intensity interferometry, Cherenkov radiation detection, or other non-astronomical uses such as solar power collection. (Note that we utilize the familiar alternate term “diaphragm” to signify the typically circular isolator located in the focal plane before a photomultiplier cell or photodiode detector. The word “aperture” has too many astronomical uses.)

A mirror surface that will satisfy an astronomical observing program will collect photons from the stellar or other program object and deliver them to the detector, yet exclude enough foreground/background photons so as to yield an acceptable signal-to-noise ratio (SNR). Herein several figures of merit are developed for light bucket mirrors dedicated to astronomical use.

We intend this chapter to be the theoretical, analytical background for our second chapter that follows in a later section of this book (Holenstein et al. 2010), and also a general contribution which applies to all highly aberrated mirrors.

Circle of Confusion

With high-quality mirrors, a standard procedure is to calculate a peak-to-valley (PV) criterion or Strehl ratio (SR) for a mirror surface. A PV value for a mirror is simply the difference between the highest and the lowest aberrated wavefront points on an optical surface; PV values of $\frac{1}{4}$ wave or better yield acceptable images for essentially all cases. A far better measure of optical surface quality is the SR, which computes

the peak intensity of the light within the Airy disk of a point source compared to the theoretical maximum delivered by an ideal optical system. An approximation to the SR is given by the Maréchal formula:

$$SR \approx 1 - (2\pi\sigma)^2 \quad (1)$$

where the root-mean-square (rms) wavefront aberration σ , is measured in waves. This form of the formula is good for SRs down to only about 0.5. Adding a few additional terms to the SR expansion does not help compute meaningful ratios when aberration is extremely large.

With light bucket telescopes collecting photons from point sources rather than from extended sources, imaging is relatively unimportant, so the foregoing mirror surface parameters are not as useful as they should be. Instead, the characterization of the point spread function (PSF) due to transverse aberrations that matters in this case is the blur-spot diameter of the program object at the focal plane, also identified as the Circle of Least Confusion or just the Circle of Confusion (CoC).

All optical systems have a certain angular resolution. The human eye, for example, has a resolution of about $1'$ for a person with 20/20 vision. The depth of field of an optical system is known from the distance that the head may move backward and forward and yet have the blur spot remain smaller than the resolution of the eye. Typically, photoelectric detectors look through focal-plane diaphragms (with or without intervening imaging) of the order of a few millimeters diameter and are used on telescopes with focal lengths of the order of meters. For example, a telescope with a focal length of 1 m with aberrations that create a blur spot of a milliradian (about $3'$) in diameter will exclude few photons that fall outside a 1 mm focal plane diaphragm. Inversely, given the focal length and mirror diameter, the problem is to characterize the maximum surface aberrations that will produce a CoC that yields an acceptable SNR when imaged on the detector.

Aberration Characterization

All mirrors are plagued by both systemic and local sources of aberration. Systemic aberrations often result from design flaws in the figuring or support of the mirror. An improperly supported mirror may, for example, have a correctible astigmatism that extends over the entire mirror surface and an improperly figured mirror may have a spherical aberration or astigmatism that can be corrected with secondary optics.

In the case of light bucket mirrors having multiple waves of aberration, coherence of the wavefront is not maintained at the focal plane. Also, reflected rays may cross, making the application of traditional Gaussian optics and Seidel aberration theory problematical (Born and

Wolf 1999, 236-244). Since the aberrations of light bucket mirrors are extensive and have varying expressions across the mirror surface, a productive way to evaluate such mirrors is with a statistical approach. This approach divides the mirror into zones, analyzes representative samples of the zones, and then collates the samples into an overall expectation of the mirror figure of merit.

In our current program, we sample the quality of zones across an unobstructed mirror surface using a right-angle Bath Interferometer, and an interferogram analysis software program called Fringe XP (Rowe 2003) is used to calculate the Zernike coefficients of the interferograms made with the device. In practice, almost any type of interferometer and fringe analysis software may be used as long as the output is a reasonable representation of the mirror figure. The Zernike coefficients are the wavefront errors (in waves) applied to the Zernike circle polynomials, the first few of which are copied into Table 1 (Wilson 2007, 288-293; Schroeder 2000, 264-265).

Table 1: Zernike Polynomials

(n,m)	Polynomial		Type
(0,0)		A_0	Piston
(1,1)	$A_1\rho\cos\theta$	$A_2\rho\sin\theta$	X, Y Axes Tilt
(1,0)		$A_3(2\rho^2-1)$	Defocus (power)
(2,2)	$A_4\rho^2\cos2\theta$	$A_5\rho^2\sin2\theta$	0°, 45° Astigmatism
(2,1)	$A_6(3\rho^2-2)\rho\cos\theta$	$A_7(3\rho^2-2)\rho\sin\theta$	X, Y Axes Coma
(2,0)		$A_8(6\rho^4-6\rho^2+1)$	Principal Spherical

In the table, a parameter pair, (n,m) , defines the form of a Zernike polynomial from the generating function (Wyant et al. 1992), A_i is the unnormalized Zernike coefficients (note that “ Z_i ” nomenclature is used in *FringeXP*), ρ is the fractional radius, and θ defines the azimuth angle about the face of the mirror. As is apparent, these low-order Zernike coefficients are useful because they correspond closely to the types of problems that mirror makers typically experience—astigmatism, coma, and spherical aberration. The *FringeXP* software also yields an rms mirror surface quality, σ , consonant with a desired conic section. Spherical surfaces are usually easier to fabricate, so for most of our explorations we have used a spherical conic section, $e = 0$.

For a spherical primary surface, the principal aberration is usually spherical, which produces a CoC between the paraxial and marginal

rays with an angular size given by (Schroeder 2000, 57):

$$\theta = 1/(128 f^3). \quad (2)$$

where f is the focal ratio. An $f/2$ spherical mirror produces spherical aberration of about a milliradian. Either a greater focal ratio or a static spherical corrector lens system may be used to minimize this systemic aberration if the conic section cannot be shifted toward a parabola.

Next, we consider the CoC caused by random mirror-height variations using geometrical optics. Light entering a telescope from infinity and striking a spherical mirror surface comes to a focus at a distance of $\approx 0.5 R_o$, where R_o is the nominal radius of curvature. However, for a real light bucket mirror, different areas of the mirror will focus light at different effective focal lengths due to the numerous aberrations afflicting it. In general, rays that strike the surface at an area experiencing $+\sigma$ waves aberration above average will come to a focus at $F_1 \approx 0.5(R_o + \sigma)$ and likewise rays that strike the surface at an area experiencing $-\sigma$ waves aberration will come to a focus at $F_2 \approx 0.5(R_o - \sigma)$. Thus, 68% of the photons striking the mirror will come to a focus within $\approx 0.5(R_o \pm \sigma)$, 95% within $\approx 0.5(R_o \pm 2\sigma)$, and 99.7% within $\approx 0.5(R_o \pm 3\sigma)$.

A rough approximation to the diameter of the CoC may be derived geometrically from the focal ratio and the multiple, n , of σ that corresponds to the desired encircled flux fraction:

$$d_{CoC, surface\ height}(n) \approx 0.5n\sigma/f \quad (3)$$

Note that there are many other aberration sources besides the normally-distributed aberration caused by surface height errors. In particular, the local slope and micro-roughness of the reflecting surface may or may not be small-amplitude Rayleigh-distributed. Errors of this kind can result from various systemic or isolated defects in the mirror shape or surface substrate. Specifically, two important manifestations of large transverse aberrations result from local slope deviations from the ideal slope in the radial and azimuthal directions. A local slope flaw with a value of $\Delta\phi$ causes photons to reflect from the local area deviated by $2|\Delta\phi|$. If the local slope aberrations are Rayleigh-distributed with root-mean-square value $|\Delta\phi|_{rms}$, 39.3%, 86.4%, and 98.9% of the flux is contained in a CoC blur spot with an angular radius of $2|\Delta\phi|_{rms}$, $4|\Delta\phi|_{rms}$, and $6|\Delta\phi|_{rms}$, respectively, for 1, 2, and 3 standard deviations in the continuous Rayleigh distribution function. The diameter of the CoC at the focal plane due to local slope transverse aberrations is

a direct function of focal length, F , and the multiple, n' , of $|\Delta\phi|_{rms}$ that corresponds to the desired encircled flux fraction and is given by:

$$d_{CoC,local slopes}(n') \approx 4n'F |\Delta\phi|_{rms}. \tag{4}$$

In order to estimate $|\Delta\phi|_{rms}$, we must first consider the formal Zernike wavefront representation.

Zernike Wavefront Representation

Each author uses his individual nomenclature and normalization for the Zernike polynomial representation. Mahajan (2007) presents the following nomenclature and equations for the wavefront as a function of the non-rotationally-symmetrical Zernike polynomials, Z_j , and expansion coefficients, a_j :

$$W(\rho, \theta) = \sum_j a_j Z_j(\rho, \theta), W(\rho, \theta) = \sum_j a_j Z_j(\rho, \theta), \tag{5}$$

where the polynomials are written:

$$Z_j(\rho, \theta) = \sqrt{n+1} R_n^0(\rho), \quad m = 0 \tag{6}$$

$$Z_{even j}(\rho, \theta) = \sqrt{2(n+1)} R_n^m(\rho) \cos(m\theta) \quad m \neq 0 \tag{7}$$

$$Z_{odd j}(\rho, \theta) = \sqrt{2(n+1)} R_n^m(\rho) \sin(m\theta) \quad m \neq 0 \tag{8}$$

The indices n and m are positive integers and also include zero, $n - m \geq 0$, and ρ, θ are defined on the unit circle. The radial polynomials are given by:

$$R_n^m(\rho) = \sum_{s=0}^{\frac{n-m}{2}} \frac{(-1)^s (n-s)!}{s! \left(\frac{n+m}{2} - s\right)! \left(\frac{n-m}{2} - s\right)!} \rho^{n-2s}. \tag{9}$$

The above representation of the Zernike polynomials is orthonormal as follows:

$$\int_0^{2\pi} \int_0^1 Z_j(\rho, \theta) Z_{j'}(\rho, \theta) \rho d\rho d\theta \bigg/ \int_0^{2\pi} \int_0^1 \rho d\rho d\theta = \delta_{jj'}. \tag{10}$$

where $\delta_{jj'}$ is the Kronecker delta function. As a result, the representation for the aberration variance is very simple:

$$\sigma_W^2 = \langle W^2(\rho, \theta) \rangle - \langle W(\rho, \theta) \rangle^2 = \sum_{j=2} \alpha_j^2. \quad (11)$$

The first fifteen Zernike orthonormal polynomials are represented in Table 2 along with the notation (Wyant et al. 1992) and the normalization factors needed for the *FringeXP* Zernike coefficients to match expansion coefficients used in equation (5).

Zernike Polynomial Gradient

The gradient vector of the wavefront representation presented in equation (5) is given by:

$$\nabla W(\rho, \theta) = \frac{\delta W}{\delta \rho} \mathbf{e}_\rho + \frac{1}{\rho} \frac{\delta W}{\delta \theta} \mathbf{e}_\theta \quad (12)$$

where \mathbf{e}_ρ and \mathbf{e}_θ are the unit vectors in the radial and azimuthal directions respectively. The mean-square wavefront gradient norm over the unit circle is:

$$\langle \|\nabla W\|^2 \rangle = \frac{1}{\pi} \int_0^{2\pi} \int_0^1 \|\nabla W\|^2 \rho d\rho d\theta. \quad (13)$$

The physical rms transverse gradient of the surface aberrations is found from the following equation:

$$|\Delta\phi|_{rms} = \frac{\|\nabla W\|_{rms}}{D/2}, \quad (14)$$

where D is the diameter of the mirror or zone that can be tested. Both the numerator and the denominator must be expressed in the same units, for example, waves. Substituting into equation (4), one finds that the local slope-induced CoC is then:

$$d_{CoC, local slope} \approx \frac{4n'F \|\nabla W\|_{rms}}{D/2} = 8n'f \|\nabla W\|_{rms}, \quad (15)$$

where the rms gradient is given in units of distance over the unit circle, usually in waves.

Estimation of $\|\nabla W\|_{rms}$ is eased with the recognition by Southwell (1982) that the gradients of higher Zernike terms in equations (6), (7), and (8) may be expressed in terms of lower Zernike polynomial terms. The integration over the unit circle of the square of the norm in equation (13) then is simplified by the orthonormality relationship expressed in equation (10).

A direct calculation of the individual Zernike gradients using Cartesian coordinates is found in Table 8.3 of Hardy (1998, 277-279). Braat

(1987) provides a direct derivation for the variance of the transverse gradient norm in terms of Zernike coefficients. Braat’s equation B3 is expressed as follows using terms and normalizations compatible with equations (5) through (9) in this chapter and Table 2:

Table 2: Orthonormal Zernike Polynomials							
<i>J</i>	<i>n</i>	<i>m</i>	Type	Orthonormal Polynomial	<i>FringeXP</i>		
					(<i>n</i>, <i>m</i>)	Coefficient	Normalization
1	0	0	Piston	1	(0,0)	Z_0	1
2	1	1	X Axis Tilt	$2\rho \cos\theta$	(1,1)	Z_1	1/2
3	1	1	Y Axis Tilt	$2\rho \sin\theta$	(1,1)	Z_2	1/2
4	2	0	Defocus (power)	$\sqrt{3}(2\rho^2 - 1)$	(1,0)	Z_3	1/√3
5	2	2	45° Astigmatism	$\sqrt{6}\rho^2 \sin 2\theta$	(2,2)	Z_4	1/√6
6	2	2	0° Astigmatism	$\sqrt{6}\rho^2 \cos 2\theta$	(2,2)	Z_5	1/√6
7	3	1	Y Coma	$\sqrt{8}(3\rho^2 - 2\rho) \sin\theta$	(2,1)	Z_6	1/√8
8	3	1	X Coma	$\sqrt{8}(3\rho^2 - 2\rho) \cos\theta$	(2,1)	Z_7	1/√8
9	3	3	30° Trefoil	$\sqrt{8}\rho^3 \sin 3\theta$	(3,3)	Z_9	1/√8
10	3	3	0° Trefoil	$\sqrt{8}\rho^3 \cos 3\theta$	(3,3)	Z_{10}	1/√8
11	4	0	Principal Spherical	$\sqrt{5}(6\rho^4 - 6\rho^2 + 1)$	(2,0)	Z_8	1/√5
12	4	2	0° Secondary Astigmatism	$\sqrt{10}(4\rho^4 - 3\rho^2) \cos 2\theta$	(3,2)	Z_{11}	1/√10
13	4	2	45° Secondary Astigmatism	$\sqrt{10}(4\rho^4 - 3\rho^2) \sin 2\theta$	(3,2)	Z_{12}	1/√10
14	4	4	0° Tetrafoil	$\sqrt{10}\rho^4 \cos 4\theta$	(4,4)	Z_{16}	1/√10
15	4	4	22.5° Tetrafoil	$\sqrt{10}\rho^4 \sin 4\theta$	(4,4)	Z_{17}	1/√10

$$\begin{aligned}
\langle \|\nabla W\|^2 \rangle = & \sum_{l=1}^{\infty} 8l \left[\sum_{i=1}^{\infty} \sqrt{2i+1} a_{2i}^0 \right]^2 + \\
& + \sum_{m=1}^{\infty} \left\{ m \left[\sum_{i=0}^{\infty} \sqrt{2(2i+m+1)} a_{2i+m}^m \right]^2 + \right. \\
& \left. + \sum_{i=1}^{\infty} 2(2l+m) \left[\sum_{i=i}^{\infty} \sqrt{2(2i+m+1)} a_{2i+m}^m \right]^2 \right\}. \quad (16)
\end{aligned}$$

With normalizations appropriate for the *FringeXP* program, the rms wavefront gradient is estimated using the first eleven Zernike coefficients by:

$$\begin{aligned}
\|\nabla W\|_{rms} \approx & [Z_1^2 + 2Z_1Z_6 + Z_2^2 + 2Z_2Z_7 + \\
& + 8Z_3^2 + 16Z_3Z_8 + 2Z_4^2 + 2Z_5^2 + 7Z_6^2 + \\
& + 7Z_7^2 + 24Z_8^2 + 3Z_9^2 + 3Z_{10}^2]^{\frac{1}{2}}. \quad (17)
\end{aligned}$$

To reduce the effects of local slope errors on the CoC, a fast design may be chosen if it may be assumed that the spherical aberration identified in equation (2) can be correspondingly reduced or eliminated by secondary optics. In any case, the diameters of the CoC given in equations (3) and (4) must be interpreted as lower limits to actual experience in the lab or dome or field.

One can specify the approximate wavefront aberration limit due to surface height flaws as follows:

$$\sigma_{\text{limit}} \approx 2fd_{\text{Aperture}}/n. \quad (18)$$

So in order to concentrate 99.7% of a source's photon flux within the blur circle falling on the detector for a detector diaphragm of 1.0 mm and focal ratio of 2.0, an astonishing 1.3 mm rms of smooth aberration is permissible. Such a value corresponds to 2,600 waves at 500 nm. For the local slope aberrations case, the rms wavefront gradient norm limit is the following:

$$\|\nabla W\|_{rms,limit} \approx \frac{d_{\text{Aperture}}}{8n'f}. \quad (19)$$

In this case, for the same detector diaphragm, wavelength, and focal ratio, the rms gradient norm limit is about 42 waves in order to concentrate 98.9% of a source's photon flux within the blur circle falling

on the detector. This latter design criterion is generally harder to meet than the olimit, especially for mirrors with surface ripples, except in the case of high-quality, tessellated mirrors which may be mounted at different heights.

Until the actual PSF of the optical system is measured, a design factor of 5 to 10 should be factored into the calculated upper limit of the aberrations because of the unknown surface contributions to them. In the example given, the design limit should be 300 to 600 waves rms surface height aberrations, with a rms gradient norm of just 4 to 8 waves for a light bucket mirror. For star fields at high galactic latitudes and for programs concentrating on bright objects, the optical system just characterized will be sufficient to avoid accidental errors due to overlapping focal plane images. Even with panoramic detectors and with the same constraints, this conclusion remains unchanged.

Figures of Merit

For a given optical configuration and detector diaphragm, how will mirror aberration affect the SNR of program object measurements? It is necessary to consider the program object photons that are counted compared to the counts of the shot noises from the star and sky foreground/background, detector noise, and scintillation (Schroeder 2000, 433; Howell 2006, 73-77):

$$SNR = \frac{N_{Star+sky} - N_{sky}}{\sqrt{N_{Star+sky} + N_{sky} + N_{Detector} + S^2}}, \quad (20)$$

where the sky measure is assumed to be made with the same effective detector diaphragm as the program object, and *S* models the scintillation noise.

With the approximation provided in equation (3) for surface height aberrations, the signal from the program object alone depends on the detector diaphragm and the mirror surface quality:

$$N_{Star} = F_{Star} \operatorname{erf}\left(\frac{\sqrt{2}f d_{Aperture}}{\sigma}\right) \quad (21)$$

where the constant, F_{Star} , represents the flux collected by the telescope from the program object. The error function, *erf*, applies because equation (3) is based on a normally-distributed random variable with one degree-of-freedom.

The sky foreground/background noise flux incident on the detector diaphragm is proportional to the squared diameter of the diaphragm:

$$N_{Sky} = \pi K_{Sky} \left(\frac{d_{Aperture}}{2F} \right)^2 \quad (22)$$

where the constant, K_{Sky} , is expressed in terms of flux per steradian.

Figure 1 shows the normalized SNR as a function of surface height aberration for different size detector diaphragms used with a 1.6 m mirror having a focal length of 3.0 m at 500 nm wavelength and with a foreground/background that is bright compared to the star and detector noises.

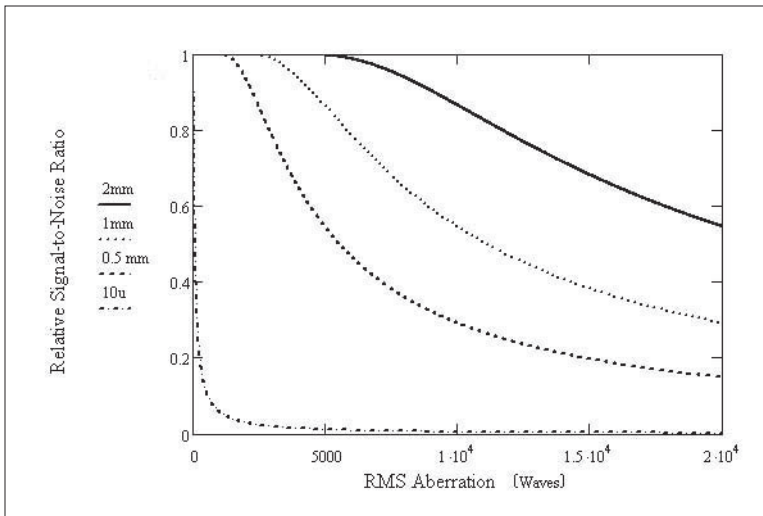


Figure 1: SNR figures of merit for sample cases of different sized diaphragms as a function of random surface height aberration where a bright point source is imaged by a 1.6 m $f/1.9$ mirror. The plots are normalized to the case of the mirror with no aberration. A similar plot may be created for the rms gradient norm aberration.

One sees from this illustration that large mirror aberrations significantly reduce the SNR compared to a perfect mirror. For example, a detector with 10 μ m pixels is totally unsuitable even when the aberration is modest unless binning, say 100 \times 100 pixels, defines the area of the CCD detector used for counts of the program object and sky background. What is particularly interesting from the figure is that there is a knee in the fall-off of SNR for relatively large amounts of mirror aberration with larger detector diaphragms. For the specific example in the figure, 2500 waves rms aberration with a 1 mm detector diaphragm yields little reduction in the SNR and 5,000 waves aberration reduces the SNR by a factor of only about

15%. For bright program objects and long integration times yielding a high intrinsic SNR, one may decide that even larger mirror aberrations are permissible.

The Full Width Half Maximum for a normally distributed variable is given by $FWHM = 2\sqrt{2\ln 2}\sigma \approx 2.35\sigma$. A Gaussian PSF is two dimensional and has a Rayleigh cumulative distribution function given by $cdf = 1 - e^{-r^2/2\sigma^2}$. Therefore, with this type of PSF form, a radius of 0.5(FWHM) (i.e., one HWHM) encircles 50%, a radius of 1.0(FWHM) encircles 93.7%, and a radius of 1.5(FWHM) encircles 99.8% of the flux. The last value is considerably less than the 3.0(FWHM) conservative value Howell (2006, 116-117) gives for 100% of the flux. No matter what the factor, for the sample case given in Howell, how does the SNR relate to diaphragm size for highly aberrated mirrors? Figures 2 and 3 are graphs of the SNR given by equation (20) for stars of different brightness for the cases of 2500 waves rms surface height and 10 waves rms wavefront gradient norm aberrations at 500 nm. The SNR is plotted as a function of detector diaphragm diameter for four different apparent brightness stars (8th, 12th, 16th, and 20th magnitudes) in relation to a 21st magnitude per square arc second background imaged by a 1.6 m $f/1.9$ mirror, a 10 second integration, and 15% overall collection efficiency. Scintillation is modeled using equation (1) of Young (1967) at an elevation of 1000 m, and an air mass of 1.5.

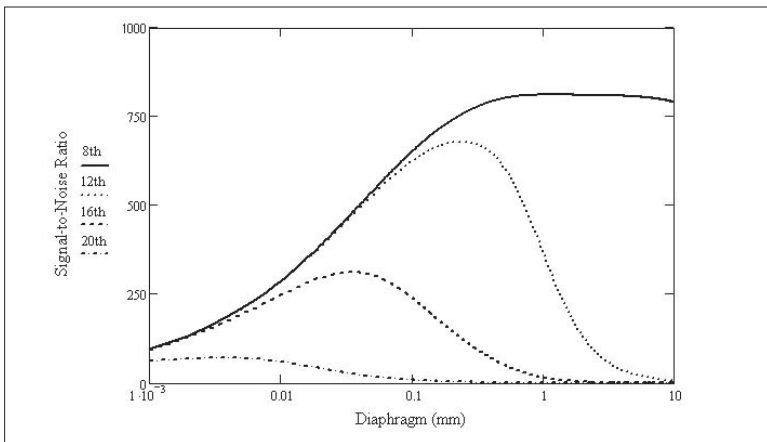


Figure 2: SNR as a function of detector diaphragm diameter for four different apparent brightness stars (8th, 12th, 16th, and 20th magnitudes) in relation to a 21st magnitude per square arc second background imaged by a 1.6 m $f/1.9$ mirror with 2500 waves rms surface height aberration. Scintillation is estimated for an elevation of 1000 m and an air mass of 1.5, with other parameters as described in the text.

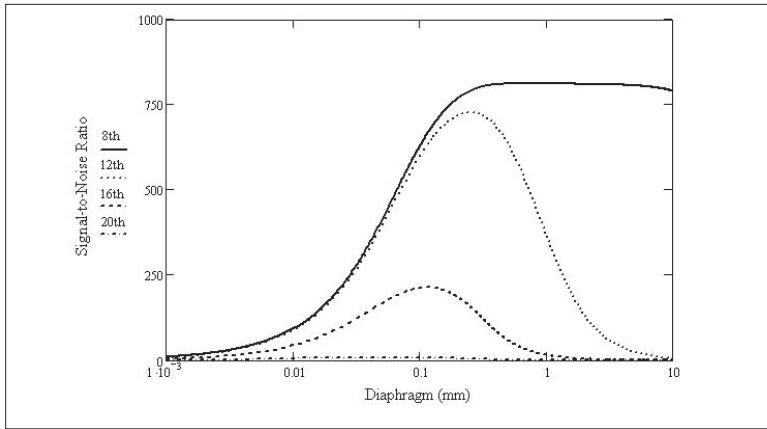


Figure 3: SNR as a function of detector diaphragm diameter for four different apparent brightness stars (8th, 12th, 16th, and 20th magnitudes) in relation to a 21st magnitude per square arc second background imaged by a 1.6 m $f/1.9$ mirror with 10 waves rms gradient norm aberration. Scintillation is estimated for an elevation of 1000 m and an air mass of 1.5, with other parameters as described in the text.

For both forms of aberration shown in Figures 2 and 3, the SNR grows as the diaphragm increases but eventually turns over as the shot noise contribution from the sky overtakes the signal flux. The plots for the fainter objects illustrate that light bucket mirrors are not desirable for use with low contrast objects. The SNR of near 750 for a 1 mm diaphragm with a bright object drops by about 50% for an object 4 magnitudes fainter. Note that the peak SNR moves to the left in the direction of smaller diaphragms for fainter objects, much as a damped harmonic oscillator experiences a frequency increase. For variable star radiometry a compromise between detector diaphragm sizes for the star, comparison, and check stars must be struck if the stars differ in brightness by considerable amounts.

Combining Results

In order to use equations (3) and (4), actual light bucket mirrors may need to be analyzed in zonal areas and then the results combined mathematically. Uncorrelated waveform aberrations add in quadrature. The overall rms waveform aberration may be calculated from the contributions of various interferograms taken over subareas, A_s , of the mirror surface, adjusted to the interferogram taken at the center:

$$\sigma_{Overall}^2 = \frac{\pi D^2}{4} \frac{\sum_{All\ subareas} \sigma_{Subarea}^2 A_s}{\sum_{All\ subareas} A_s} \quad (23)$$

An alternate approach using the blur spots of zonal regions may be added as follows:

$$d_{CoC,Overall}^2 = \frac{\pi D^2 \sum_{All\ subareas} d_{CoC,Subarea}^2 A_S}{4 \sum_{All\ subareas} A_S} \quad (24)$$

Use of equation (24) requires that the focal ratios of the individual zones, and not the entire mirror, be used in equations (3) and (4).

Note that actual results of using equations (23) and (24) will vary depending on the degree to which the aberrations of different zonal subareas are in fact independent and add in quadrature.

An overall strategy for light bucket mirrors is to use the focal ratio which minimizes equation (24) for the main highly aberrated primary mirror, and then to use high quality focal reducer and spherical corrector optics to improve the character of the PSF. For instance, using a $f/2$ spherical mirror instead of a $f/4$ spherical mirror will reduce the CoC blur spot caused by local slope aberration issues by a factor of two, but it will also increase the spherical aberration by a factor of 2^3 , or 8. Figure 4 shows the effect of a combined CoC blur spot from spherical, surface height, and local slope aberrations as a function of focal ratio.

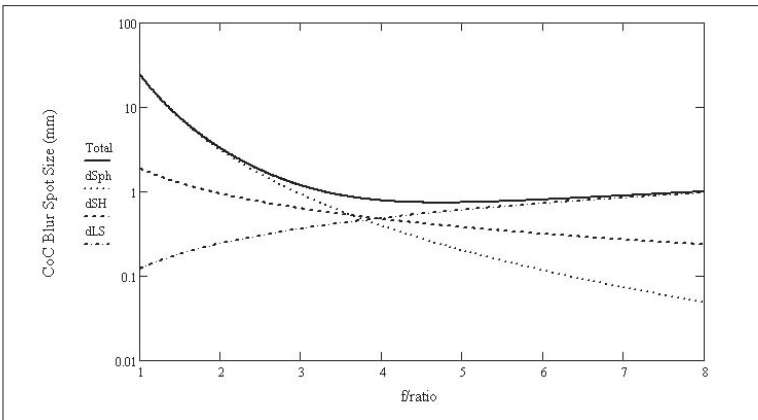


Figure 4: CoC blur spot size as a function of $f/ratio$ for a 1.6 m spherical mirror with 2500 rms waves of surface height and 10 rms waves of gradient norm local slope aberrations. The symbols dSph, dSH, and dLS are the CoC blur spots from spherical, surface height, and local slope aberrations, respectively, and the total aberration includes all three sources added in quadrature. The surface height and the local slope CoC blur spots are three standard deviation sizes.

Figure 4 shows that systemic spherical aberration dominates the CoC blur spot size without secondary correcting optics for this example.

The crossover between surface height and local slope aberrations moves to the left as surface height aberrations diminish.

Secondary optics which correct for systemic spherical aberration may be much easier to fabricate than secondary optics for complicated surface height and local slope aberrations if the resultant CoC blur spot is still larger than the desired tolerance limit.

Also, note that high frequency surface defects, such as microripples causing diffuse reflection, do not have a ready solution. One must select the best substrate possible and polish out these problems if possible. In other words, light bucket mirrors may have considerable low-spatial frequency problems of manufacture or support which are fixable by mechanical adjustments of the primary mirror and/or secondary static-, active-, or adaptive-optics of one form or another. High-spatial frequency problems, on the other hand, have no ready solution which is economical in comparison to the cost of the light bucket mirror itself.

Telescope Tracking Errors

Telescope tracking errors make a program object drift across or even out of the detector diaphragm. Software that processes a CCD image may be able to compensate by moving the readout window on succeeding images. In contrast, diaphragm photometry with a single photodiode or photomultiplier detector will suffer unless re-centering of the program object occurs frequently. This is inherently a mechanical/electrical problem and not an optical one.

For light bucket mirrors the PSF extends far beyond the Airy disk. Figure 5 illustrates how flux is lost on one side yet gained on the other side of a drifting circular-shaped diaphragm.

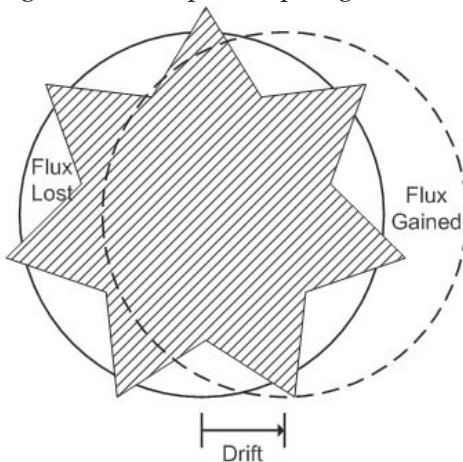


Figure 5: A circular diaphragm gains some program object flux as it drifts due to tracking errors. However, more flux is lost than gained due to the drift so there is always a net decrease in program object flux.

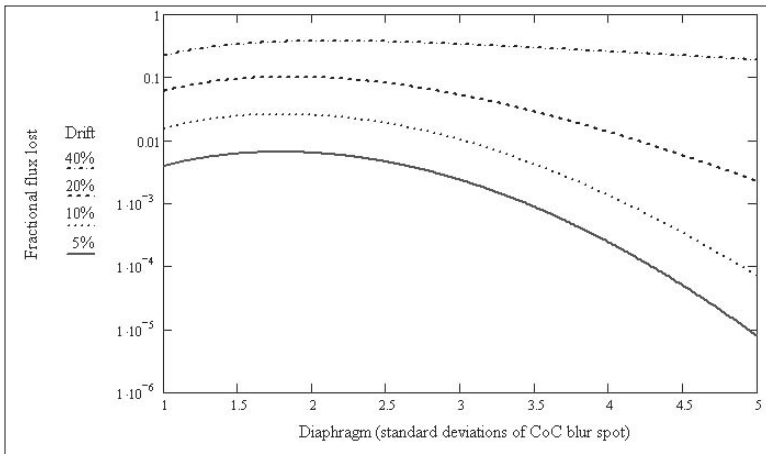


Figure 6: Fraction of flux lost in a circular diaphragm due to centering-drift errors at the focal plane as a function of diaphragm size in standard deviations of CoC aberration from a Gaussian PSF. The drift is expressed as a percentage of the diameter of the detector diaphragm.

Figure 6 shows the flux deficit that results from centering errors of a circular diaphragm as a function of diaphragm size and drift of the program object from the center of the diaphragm.

The figure shows that the fraction of flux lost initially increases with diaphragm size due to drift in an absolute sense also increasing (i.e. as a percentage of diaphragm diameter). The fraction of flux lost turns over rapidly as the diaphragm increases in size beyond two standard deviations of the CoC blur spot. For a mirror with a focal ratio of 2.0, and 15 waves rms local slope aberration at 500 nm, equation (15) gives the one standard deviation CoC as 0.12 mm. So, a diaphragm of 4 standard deviations is 0.5 mm and still yields less than 0.1% (i.e. one milli-magnitude) flux loss when the drift is about ten percent during the detector integration. However, if the drift in this example is allowed to extend to 20%, about 1.0% of flux is lost.

Conclusions

- Light bucket mirrors challenge traditional aberration analysis used for diffraction-limited general-purpose telescope mirrors. A statistical approach is needed to characterize performance properly.

- For a detector diaphragm of 1.0 mm and a telescope focal ratio of 2.0, a maximum of about 1.0 mm rms of smooth surface height aberration and 42 waves rms of local slope aberration is permissible for about 99% of a point source's flux to be collected.

- Large mirror aberrations significantly reduce the SNR of collected flux. The peak in SNR occurs at a detector diaphragm diameter considerably less than the size for collecting 99% of the source flux. Light bucket mirrors are not suitable for imaging applications nor are they desirable for use with low contrast objects.

- CoC blur spots from surface height flaws and local slope figuring issues may be quantified by combining interferometer results from multiple areas.

- Telescope tracking requirements are relaxed due to the large detector diaphragms used with light bucket mirrors.

Acknowledgements

The authors wish to thank editor Russ Genet and some members of the Alt-Az Initiative for suggestions and feedback on the contents of this text.

References

Born, M. and Wolf, E. 1999. *Principles of Optics, 3rd ed.* Cambridge: Cambridge U. Press.

Braat, J. 1987. Polynomial expansion of severely aberrated wave fronts. *J. Opt. Soc. Am., A4*, 643-650.

Genet, R. 2009. Lightweight mirror developments. Presented at the Society for Astronomical Sciences 28th Annual Symposium on Telescope Science.

Hardy, J. W. 1998. *Adaptive Optics for Astronomical Telescopes.* New York: Oxford University Press.

Holenstein, B. D., Mitchell, R. J., Holenstein, D. R., Iott, K. A., and Koch, R. H. 2010. Experiments with pneumatically-formed metalized polyester mirrors. In *The Alt-Az Initiative: Telescope, Mirror, and Instrument Developments*, eds. Genet, R., Johnson, J., and Wallen, V. Santa Margarita, CA: Collins Foundation Press.

Howell, S. B. 2006. *Handbook of CCD Astronomy, 2nd ed.* Cambridge: Cambridge U. Press.

Mahajan, V. 2007. In *Optical Shop Testing, 3rd edition*, ed. D. Malacara, 516-518. Hoboken WI: Wiley.

Rowe, D. 2003. *FringeXP: A Fringe Analysis Program, Ver. 2.* Internet <<http://www.ceravolo.com/fringeXP.html>> accessed 27 January 2010. Note that *OpenFringe* is an open source variant that is available at Internet <<http://sourceforge.net/projects/openfringe/>>.

Schroeder, D. J. 2000. *Astronomical Optics.* New York: Academic Press.

Southwell, W. H. 1982. What's wrong with cross coupling in modal wave-front estimation? *Proc. SPIE, 365*, 97-104.

- Wilson, R. N. 2007. *Reflecting Telescope Optics I: Basic Design Theory and Its Historical Development*, 2nd ed. New York: Springer-Verlag.
- Wyant, J. and Creath, K. 1992. In *Applied Optics and Optical Engineering*, Vol. XI, ed. R. Shannon and J. Wyant, 1-39. New York: Academic Press.
- Young, A. T. 1967. Photometric error analysis. VI. Confirmation of Reiger's theory of scintillation. *AJ*, 72, 747-753.